

Automatic Input Feature Relevance via Spectral Neural Networks

Lorenzo Chicchi^{1,*}, Lorenzo Buffoni¹, Diego Febbe¹, Lorenzo Giambagli¹, Raffaele Marino¹, and Duccio Fanelli¹

¹Department of Physics and Astronomy, University of Florence, Sesto Fiorentino, Italy , INFN, Italy

*lorenzo.chicchi@unifi.it

ABSTRACT

In machine learning practice it is often useful to identify relevant input features, so as to obtain compact dataset for more efficient numerical handling. On the other hand, by isolating key input elements, ranked according their respective degree of relevance, can help to elaborate on the process of decision making. Here, we propose a novel method to estimate the relative importance of the input components for a Deep Neural Network. This is achieved by leveraging on a spectral re-parametrization of the optimization process. Eigenvalues associated to input nodes provide in fact a robust proxy to gauge the relevance of the supplied entry features. Notably, the spectral features ranking is performed automatically, as a byproduct of the network training, with no additional processing to be carried out. The technique is successfully challenged against both synthetic and real data.

1 Introduction

Deep Neural networks (DNNs)¹⁻⁵ are among the most popular machine learning tools, and, as such, routinely employed in a vast plethora of applications⁶⁻⁹. As for other machine learning techniques, and when employed for e.g. classification and/or regression tasks, DNNs can automatically extract valuable information from the supplied input vector. This amounts to isolate crucial components to implement unmanned decision making strategies. In many cases of interest, input data are multidimensional. In general, it is hence difficult to selectively identify the subset of attributes which prove crucial for the analysis. To identify key input features could be indeed relevant for (i) devising apt solutions for data compression and compactification; (ii) providing critical insights into the processes that led to the produced output.

A first solution is to operate an a priori feature selection, with the aim to isolate beforehand a limited subset of supposedly relevant input elements that should undergo subsequent scrutiny¹⁰. This is certainly useful to reduce the size of the input to be eventually processed. On the other hand, by clipping part of the dataset, a non zero risk always exists that could yield an unpredictable loss of performance for the trained network. This is as opposed to other viable approaches designed so as to preserve the total amount of information across training.

Among the methods proposed to shed light on the pathways that form the basis of decision of a trained model, worth mentioning is the so called Layer-Wise Relevance Propagation method^{11,12}. This latter implements a backpropagation, from the output to the input space, to reach the relevant features that are provided at the entry layer. The method has been successfully challenged against distinct domains of application^{13,14}. Reference should also be made to SHAP¹⁵ (SHapley Additive exPlanations) a game theoretic approach based on the classic Shapley values, which connects optimal credit allocation to local output explanation. Other examples include - but are not limited to - the techniques identified via the compact acronyms IG, DeepLIFT, LIME¹⁶⁻²¹. To the best of our knowledge, the vast majority of existing methods are however input-dependent. As such, they require a certain number of operations to be carried out after training, for each examined input, so as to assess the relevance of the features for any given supplied item.

Here, we put forward a different method which yields a global metric to assess the relevance of input features to a general feedforward neural network. The procedure applies to the whole dataset and not just to individually examined items. Furthermore, the evaluation of the features is obtained as a byproduct of the training with no additional processing to be carried out. At the end of the training a ranking of the supplied feature is returned, as determined by a set of scalar parameters (one for each distinct feature provided as an input). As mentioned, and unlike the aforementioned methods, the proposed metric is not input dependent. At variance, it provides a global insight on how the model oversees the input space, upon learning. Also, and as opposed to standard techniques for input feature selection, the analysis is not conducted a priori on the data to be eventually scanned.

To reach this goal, we will make use of a recently introduced scheme for handling the optimization of feedforward networks, known as *spectral parametrization*²²⁻²⁷. The mathematical foundation of the spectral methodology lies within the theory of

networks. From this angle, feedforward neural networks can be pictured via a dedicated spectral decomposition that materializes, in direct space, in a collection of adjacency matrices for the linear mapping of the signal across adjacent layers. As we shall argue, the optimized eigenvalues, as made accessible at the end of the training, will return an automatic and self-consistent ranking of the individual input features.

The paper is organized as follows. In the next Section we will review the mathematical basis of the spectral approach to neural network training and introduce the proposed ranking strategy. Then, we will turn to discussing a first application to independent and correlated Gaussian data. These are mock data, with different level of complexity, to be regressed by the spectral neural network. In the subsequent Section the proposed method is challenged against the celebrated MNIST database, operated in different modalities. As we will show, the spectral based feature detection method is able to isolate a subset of relevant pixels that prove central for image classification. Then, we turn to challenging the method against an additional dataset, made of stellar spectra. The goal here is to obtain information on relevant frequency bands for the assessment of stellar metallicity. Finally, we sum up and draw our conclusions.

2 On the spectral parametrization

Let us begin by reviewing the basic of the spectral method²². We denote with $l-1$ and l two consecutive layers of a feedforward neural network. Assume the layers to be respectively composed by N and M nodes. The vector $\mathbf{x}^{l-1} = (x_1^{l-1}, \dots, x_N^{l-1})$ (resp. $\mathbf{x}^l = (x_1^l, \dots, x_M^l)$) stores information on the activity of the nodes belonging to layer $l-1$ (resp. l). The linear transfer between the two adjacent layers is operated by a rectangular $M \times N$ matrix W , whose elements read w_{ij} . Hence, $\mathbf{x}^l = f(W\mathbf{x}^{l-1})$, where f is a non-linear filter. Under the spectral paradigm, the above operation can be recast in an equivalent form that assumes dealing with the bipartite direct network made of the $N+M$ nodes involved in the transfer. The state vector at the departure layer can be written as $\mathbf{z}^{l-1} = \mathbf{x}^{l-1} = (x_1^{l-1}, x_2^{l-1}, \dots, x_N^{l-1}, 0, 0, \dots, 0)$ where we made explicit that the non trivial activity is solely localized on the nodes of the first layer. Then, $\mathbf{z}^l = f(A\mathbf{z}^{l-1})$, where the last M elements of vector \mathbf{z}^l refer to the activity on the destination layer; A is a $(M+N) \times (M+N)$ matrix with a $M \times N$ sub-diagonal block that coincides matrix W , as illustrated in the Methods section. It should be noted that the diagonal entries of matrix A do not reflect on the produced activity on layer l , see Figure 1. One can hence invoke a spectral decomposition of the square transfer matrix, as $A = \Phi \Lambda \Phi^{-1}$ where (i) Φ , the matrix of the eigenvectors, is lower-block triangular with ones on the diagonal, (ii) Λ identifies the diagonal matrix formed with the eigenvalues $(\lambda_i, i = 1, \dots, N+M)$ of A . Given the specific form of matrix Φ , it can be shown^{23,26} that $\Phi^{-1} = 2\mathbb{I} - \Phi$. In practical terms, the elements of A , namely those involved in the self-consistent definition of the relevant transfer matrix W , can be written as a function of the eigenvalues λ_i and the non trivial entries ψ_{ij} of the eigenvector matrix Φ . An explicit calculation can be performed that yields $w_{i \rightarrow j} = w_{ji} = (\lambda_i - \lambda_j) \psi_{ji}$, where $i = 1, \dots, N$ refer to nodes located on layer $l-1$ and $j = 1, \dots, M$ to those assigned to layer l . Further technical details are provided in the Methods section. A direct correspondence can be hence drawn between individual eigenvalues and nodes within the sampled collection. Training a feedforward network under the spectral standpoint amounts to minimize the loss (a suitable metric that gauges the distance between produced and expected output at the exit layer) with respect to the eigenvalues and eigenvectors. In light of the existing correspondence, the magnitude of the optimized eigenvalues can be used as a reliable marker of the nodes' relevance, an idea that has been explored in^{23,26,27}. An effective trimming strategy was in particular proposed in²⁶ which enables for the trained network to be considerably shrunk in size by removing nodes flagged as unimportant. By leveraging on the eigenvalues and their associated magnitudes, it was possible in²⁷ to estimate the hidden dimension of the target objective function. By expanding further on these ideas, we will hereafter propose an effective input feature detection algorithm. To this end, we chose to operate under the simplifying assumption $\lambda_j = 0$ (i.e. by forcing to zero the eigenvalues associated to destination nodes) yielding:

$$w_{ji} = \lambda_i \psi_{ji}. \quad (1)$$

The spectral rewriting of the inter-nodes weights w_{ij} yielded therefore a factor, the eigenvalue λ_i , which multiplies all the links emanating from the departure node i . The larger the magnitude of the optimized λ_i the more relevant the associated node i for the processing of the information across the network. Building on this observation, we will show that the trained eigenvalues associated to the starting layer $l=1$ can be effectively employed to automatically discriminate between irrelevant and relevant input features. More specifically, we will demonstrate, that eigenvalues (multiplied by the norm of the corresponding eigenvector entry) can be exploited to rank the relative importance of the features otherwise deemed as irrelevant. The method will be tested against classification problems constructed from mock and real datasets. For all examined cases, a penalty is added to the loss function as in the spirit of^{27,28}. This is a L_2 regularization of λ_i which forces eigenvalues associated with irrelevant components to be set to zero (and not just left unaltered to their initial values, possibly drowned in the sea of their relevant homologue). It is worth stressing that in principle it is enough to have just the first layer parameterized as spectral for this analysis to apply. For further details on the training procedure refers to the Methods section.

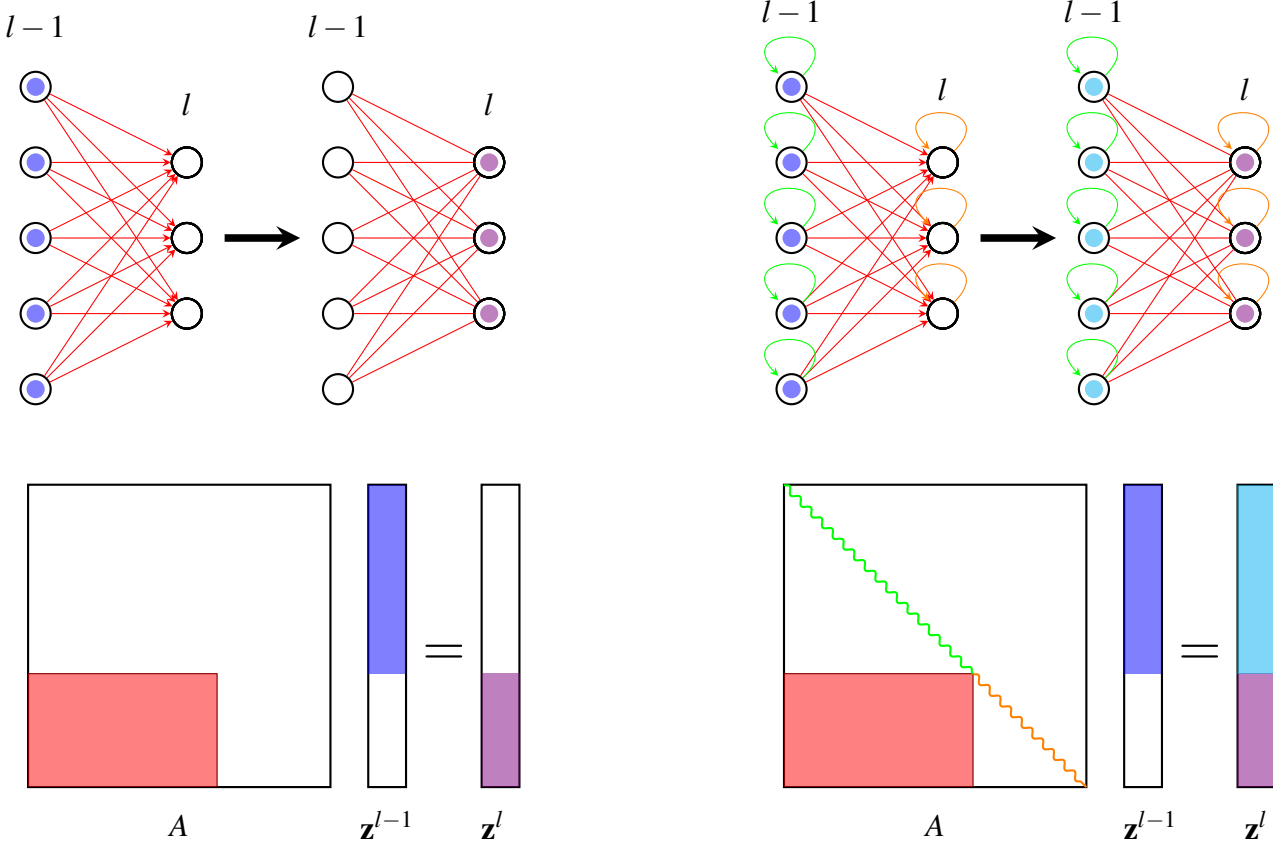


Figure 1. The linear information flow for a modified network with the inclusion of diagonal entries (eigenvalues) in the triangular matrix A . The eigenvalues introduce self-loops (as depicted on the right), and this is at variance with the usual setting without loops (on the left). Notice that the bottom elements of \mathbf{z}^l are identical in both cases, yielding exactly the same activation vector upon linear transfer

3 Numerical experiments

The method discussed above for input feature detection is hereafter challenged against different datasets. We will begin in particular by considering a simple multidimensional Gaussian dataset with independent entries. Then, we will turn to considering mock data generated from correlated Gaussian variables. After that, we will move forward to work with the celebrated MNIST dataset and, finally, we will focus on an experimental catalogue of stellar spectra relevant for astrophysical applications

3.1 Independent Gaussian distributions dataset

The first dataset is structured with 2 target classes and input vectors with 20 independent features. Each data component is sampled from a Gaussian distribution, see Fig. 2. While some components are drawn from distributions which are set to be identical across classes, others display only partial overlap. Components with identical distributions offer no discriminatory information. As such, they prove ineffective for classification purposes. Conversely, the other components are pivotal, the smaller the overlap the larger their relevance in promoting the sought discrimination.

A spectral feedforward neural network, parametrized as stipulated by Eq. (1), has been trained with the aim of assigning input from the above dataset to the correct class of origin. The employed network consists of three hidden layers with, respectively, 100, 100, and 50 neurons. In addition, the network accommodates for an input layer of size 20 and an output layer of size 2. At the end of the training, we analyzed the 20 eigenvalues, associated with the input layer as in the spirit of the above discussion (with an abuse of language we will from here on call eigenvalues the rescaled version of this latter which incorporate the norm of the eigenvectors, as stipulated in the Methods section). As shown in the left panel of Fig. 3, eigenvalues entangled with irrelevant features are all zero, while eigenvalues which can be traced back to relevant input components are non-zero. Hence, the eigenvalues associated to the input layer can efficiently tag features identified as relevant by the network itself to solve the assigned task. The magnitude of non-zero eigenvalues, i.e., those associated with relevant components, is found to

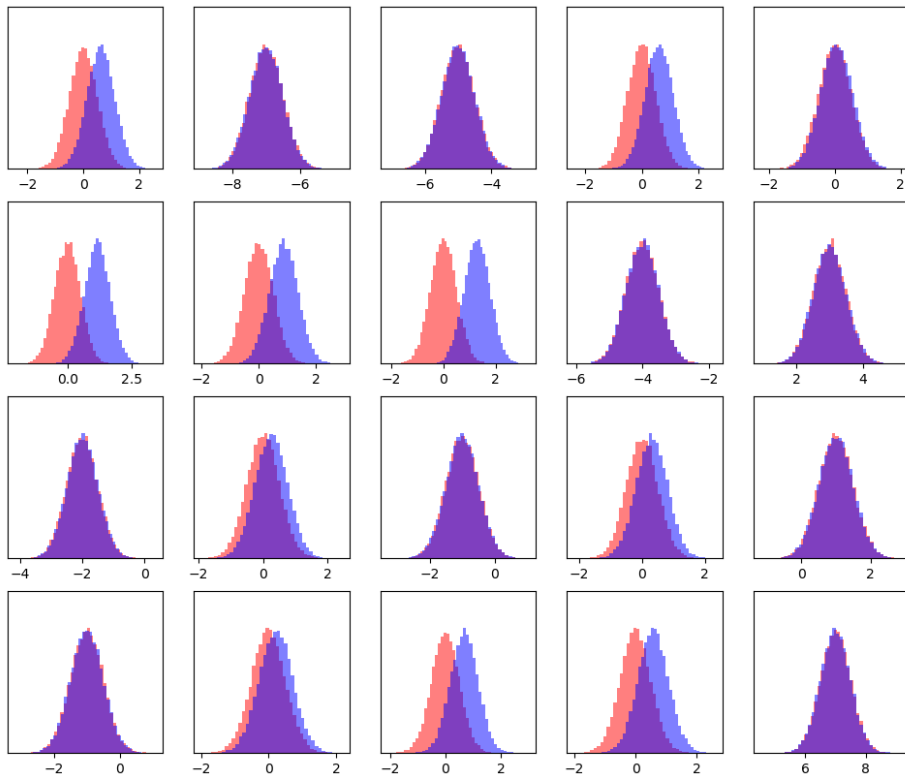


Figure 2. Input vector components distributions. Distribution of the values of the 20 components of the input vectors. The distributions for the data belonging to the first (resp. second) class are represented in red (resp. blue). For some components, the two classes are indistinguishable, while in some other cases the two distributions are only partially overlapping.

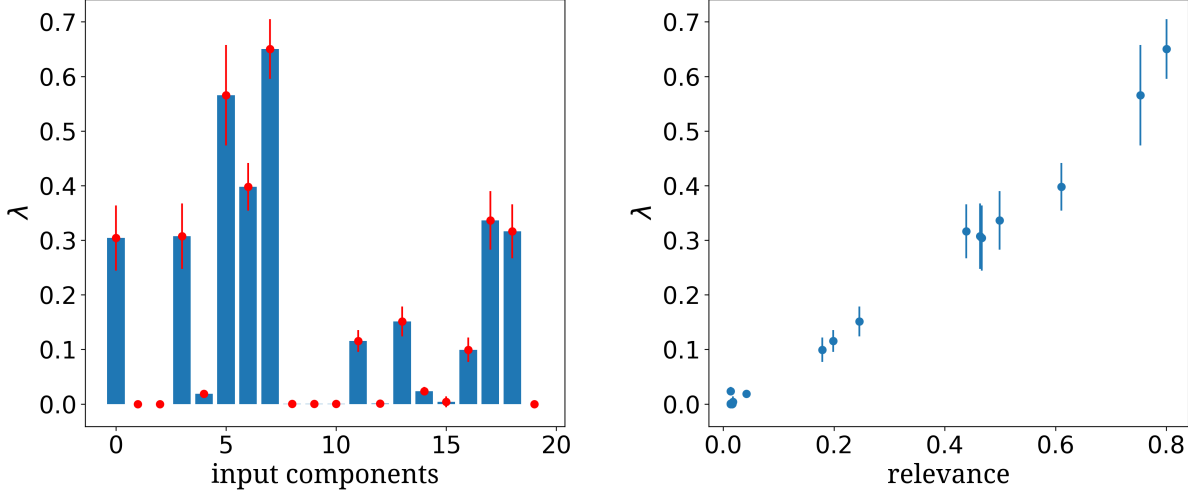


Figure 3. The left panel displays the 20 post-training eigenvalues associated to the input layer, for the *simple Gaussian dataset*. The red dots and the red bars correspond to the average values and the standard deviations of the results obtained by repeating the experiments for 10 independent realizations. In the right panel, the same post-training eigenvalues are reported against a relevance parameter that gauges the distance between the distributions (respectively blue and red, in Fig. 2) from which the components are eventually drawn. The distance is defined as the absolute value of the difference between the two means.

correlate with a direct measure of the relative distance between the distributions from which individual components are drawn (see the right panel of Fig. 3). Since the distributions differ only in their mean value, we quantify the above distance as the absolute value of the difference between the two means.

3.2 Correlated Gaussian distributions dataset

Unlike the dataset just analyzed, real datasets often exhibit correlations between input vector components, and crucial task-solving information are frequently concealed within those correlations. With this motivation in mind, we tested the proposed spectral feature detection method on a different dataset that contains pairwise correlations between input vector components. The dataset is still organized into two distinct classes that are to be eventually identified. Input vectors are now made of 10 components. The first 8 components are defined as follows:

$$\begin{aligned} x_{2n} &\sim \mathcal{N}(0, 1) \\ x_{2n+1} &= x_{2n} && \text{if } c(\vec{x}) = 0 \\ x_{2n+1} &= \begin{cases} x_{2n} \text{ with prob. } 1 - p_n & \text{if } c(\vec{x}) = 1 \\ -x_{2n} \text{ with prob. } p_n & \end{cases} \end{aligned} \tag{2}$$

where $c(\vec{x})$ is the target class of the input and the index $n \in \{0, 1, 2, 3\}$ denotes the four pairs. The last two components are independently drawn from two identical normal distributions $\mathcal{N}(1, 0)$ regardless of the class of belonging:

$$x_8, x_9 \sim \mathcal{N}(0, 1). \tag{3}$$

As a first noticeable observation, we remark that it is not possible to separate the two datasets by solely relying on independent observations of the respective vector components. Indeed, crucial information are reflected in how pairs of components are mutually correlated (see left panels of Fig. 4).

To better understand the relationship between the different components, let us focus on the first two entries of the input vectors, x_0 and x_1 . For data belonging to class 0 (as we label the first of the two) $x_0 = x_1$, that is, the first two components are perfectly correlated. Conversely, the two components of data belonging to the other class (denoted by 1) are equal with probability $1 - p_0$ and have opposite sign with probability p_0 . If $p_0 = 0$, the first two components are equal for both classes. No information about the class to which the supplied data belong can be thus extracted by comparing the two above components. The second component is indeed a mere copy of the first and therefore irrelevant for classification purposes. On the other hand, if $p_0 = 1$, the first and second components from class 1 data are in perfect anti-correlation, while data from class 0 are still matched and thus fully correlated. Hence, in the latter case, it is possible to completely separate the two classes by

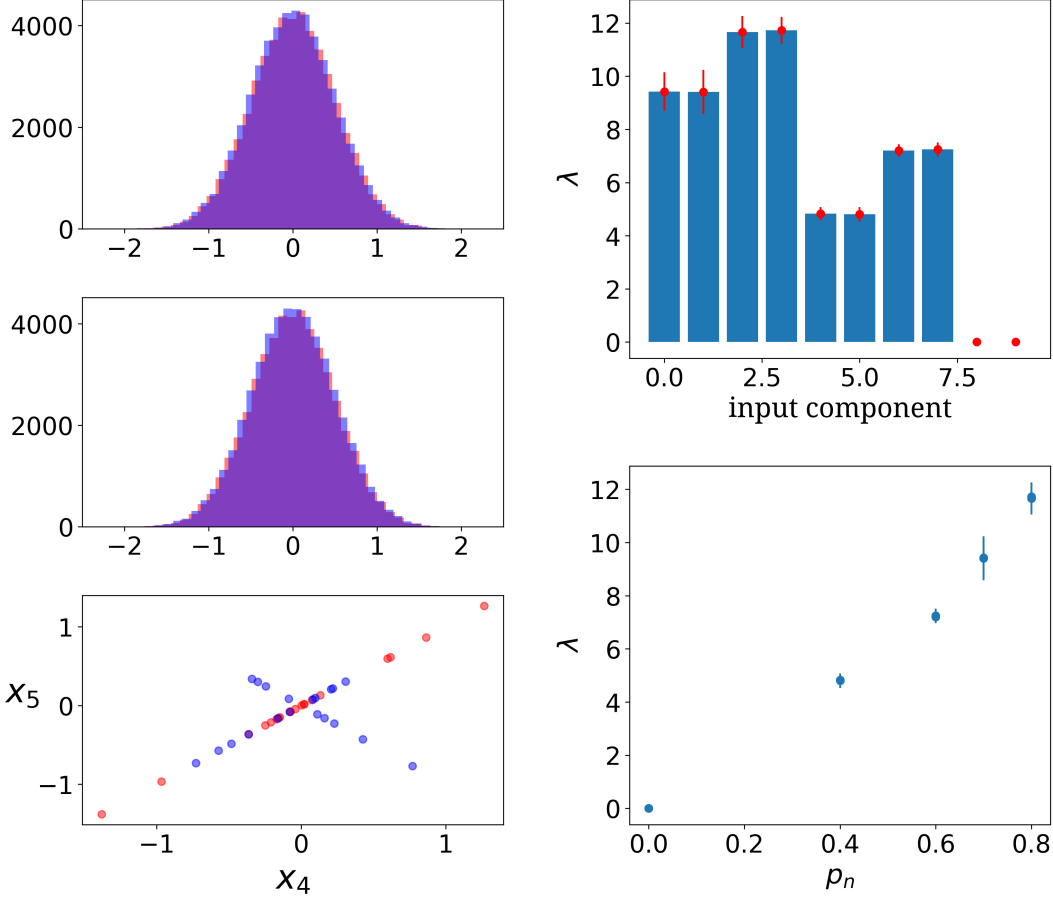


Figure 4. Left column: the distributions of the values of the fourth and fifth components of the input vectors in the *correlated Gaussian dataset* are shown in the first two panels. In the bottom-left panel, the fifth component is plotted against the corresponding fourth component for some input vectors of the same dataset. Right column: the upper-right panel reports the ten post-training eigenvalues (referred to the input layer) for the *correlated Gaussian dataset*. Red dots and red bars quantifies the recorded average values and the associated standard deviations, as obtained by averaging over 10 independent realizations. In the bottom-right panel the same post-training eigenvalues are plotted against the parameter p_n , as defined in the main text.

solely comparing x_0 and x_1 . The Parameter p_n quantifies therefore the degree of sensible information which can be pulled out from a direct comparison of the two components in the n -th pair. We want to stress that, regardless of the value of p_n , neither component individually contains information on the specific class to which the vector belongs. Therefore, useful information can be obtained to solve the classification task only by analyzing the two components simultaneously. Following this observations, we generated the dataset by using four different values of $p_n \in [0, 1]$ for the four pairs. Finally, the last two components are not correlated with the others and are identically distributed for both classes, hence void of information. We therefore assign a parameter $p_4 = 0$ to these two components to explicitly state their manifest irrelevance.

The architecture of the employed neural network, parameterized via its spectral modality, is identical to that put forward for the analysis of the uncorrelated dataset (except for the first layer that in this case receives just 10 entries). In upper right panel of Fig. 4, the post-training eigenvalues referred to the input layer are shown. Firstly, we notice that pairs are correctly spotted out, as they are assigned the very same eigenvalue entry. Moreover, eigenvalues associated with irrelevant components are tuned zero for this dataset as well, an observation that testifies again on the ability of the spectral network to discriminate between irrelevant and relevant features. Lastly, the magnitude of the recorded eigenvalues scales proportionally to the control parameter p_n , which quantifies the relevance of the selected pair for classification purposes (bottom right panel, Fig. 4). In conclusion, and also for this second, more complex dataset, the optimized eigenvalues referred to the first layer are a good proxy of the importance of the associated components.

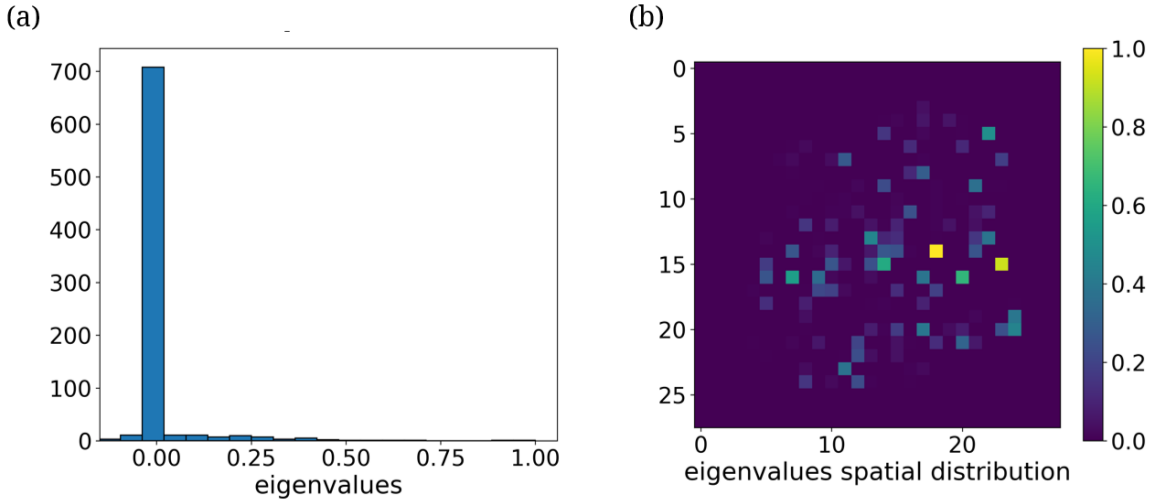


Figure 5. In panel (a) the distribution of the first 784 post-training eigenvalues (normalized to their maximum) is reported. Panel (b) shows the input space for the same dataset, where each component (i.e., pixel) is colored according to its relative post-training eigenvalue.

3.3 The MNIST dataset

As an additional test, we applied the spectral features detection method to a reduced version of the well-known MNIST dataset²⁹. This latter consists of 28×28 images depicting handwritten digits, ranging from 0 to 9, to be eventually classified. In our experiments, and to deliver a clear message, we first focused on the subset of images “zeroes” and “ones”. Despite the simplicity of the adopted framework, it is interesting to test the method against a real dataset, where the measure of the relevance of the components is not *a priori* given. The input vectors of the MNIST dataset has a dimension of 784, and each component of the vectors represents the intensity of a specific pixel in the corresponding image.

In this context, asking which component is relevant amounts to asking which pixel (or collection of pixels) discloses the information that is used by the trained network to make decision.

Once again, we trained a spectral feedforward neural network by adjusting the trainable spectral parameters. The hidden structure of the network is identical to that employed for the above applications. Clearly, the input layer is now made of 784 elements, the size of the supplied items. The exit layer is still composed of just two nodes, one associated to the images that display a zero and the other pointing to the ones. As expected, the trained model performs very well in terms of estimated classification accuracy (larger than 99 %).

The distribution of the post training eigenvalues associated to the input layer is reported in panel (a) of Fig. 5. A clear peak at zero appears, signifying that many eigenvalues have been suppressed, thus targeted as ineffective, during training stages. Just a few eigenvalues are non-zero. This conclusion can be rephrased by stating that many pixels are unnecessary for task resolution. Panel (b) of the image 5 shows the 28×28 pixels, the canvas on which images are painted, colored according to the associated eigenvalue score: blue pixels refer to smaller eigenvalues, while yellow pixels stand for large positive values.

The accuracy of the trained network gets modulated as a function of the number of input pixels included in the analysis, see Fig. 6. In this latter Figure, we progressively include more and more pixels ranked from the most to the least important, as according to the spectral (i.e. eigenvalues magnitude) metric. Remarkably the computed accuracy raises rapidly, with a sharp, almost abrupt approach to asymptotic convergence, a trend that cannot be reproduced by employing any other set of identical cardinality of randomly selected pixels. In particular, by arbitrarily fixing the number of pixels to be included (in descending order of importance) to 20, one obtains a final accuracy which is competitively close to that recorded when the full load of pixels is provided at the input layer. These 20 pixels, ranked as most important and sufficient for the correct functioning of the trained classification algorithm, can be located back on the 2D grid that defines the images support (inset in Fig. 6).

To figure out how the network exploits the subset of selected pixels for handling the classification task, we can overlay the mask containing only the relevant pixels (the binarized picture displayed as inset in Fig. 6) on individual input (images) data. A few examples of what one gets following this procedure are reported in Fig. (7). Images portraying digit “one” activate a cluster of pixels positioned in the center of the drawing (red circles), as opposed to images with a “zero” displayed, which resonate instead with a complementary set of pixels surrounding the center. The method is hence capable of identifying a minimal subset of input components which prove crucial for the correct handling of the examined data.

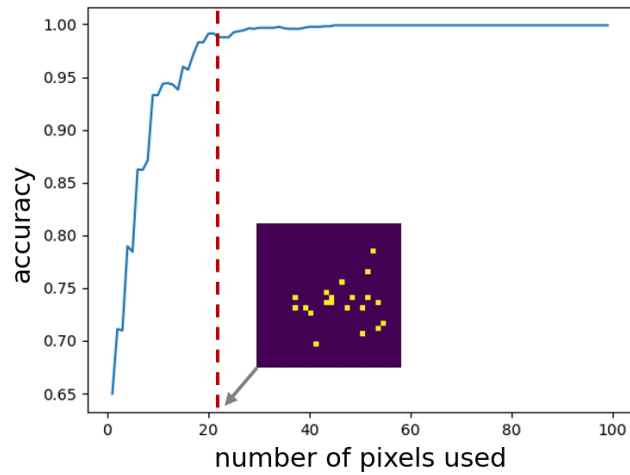


Figure 6. The blue line refers to the accuracy of the model as the number of pixels taken as input grows. The order in which the pixels are inserted follows the absolute value (magnitude) of their corresponding post-training eigenvalues. In the inset, the input space is represented, with the twenty most important pixels highlighted.

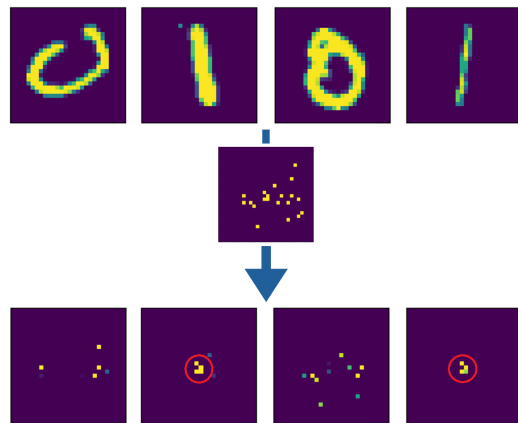


Figure 7. Four examples of images from the MNIST dataset as originally presented (top) and after the application of the mask identified by the proposed method (bottom). The red circles identify the central cluster activated by images representing a “one”.

To further elaborate on the performance of the proposed method for input feature detection, we repeat the above analysis for the subset of images relative to numbers "five" and "nine". The results are in line with those reported above, as it can be readily appreciated by visual inspection of Figure 8. With just 14 pixels ($\simeq 1.8\%$ of the total) the network achieves approximately 90% classification accuracy. These pixels are localized in the upper right portion of the image where the "nines" feature a closed circular loop, which is instead lacking in the "fives". This is hence the macroscopic distinctive attribute that is learned by the neural network to deal with the assigned task.

Finally, we also report in Figure 9 the recorded accuracy for the complete collection of digits (ranging from 0 to 9) which compose the entire MNIST dataset. Also in this case, and in analogy with the results obtained for the examined settings in which pair of digits are directly compared, the accuracy raises as a function of the number of input pixels included in the analysis, and ranked according to their spectral importance.

3.4 Stellar spectra and metallicity prediction

In this Section we report on the performance of the algorithm against a dataset of interest for astrophysics. More specifically, we consider the MILES stellar library³⁰, composed of 985 stars. The dataset is composed of stellar spectra, namely flux as a function of wavelength, in the range 3525–7500 Å. For each spectrum we consider the associated stellar parameters (effective temperature, gravity, and the abundance of heavy elements known as metallicity) from³¹. A few representative spectra are shown in Figure 10. Because of its spectral type coverage and flux calibration accuracy this stellar library has been extensively used as a basis for constructing stellar population models to analyze galaxy spectra^{32,33} and therefore deriving metallicity and star-formation histories of galaxies.

To estimate the metallicity, we here train a spectral feedforward neural network, which takes as an input the displayed intensity of the recorded spectra at various wavelengths. The network architecture consists of three hidden layers comprising 200, 50, and 50 neurons, respectively. As in the spirit of the above, the spectral ranking of the supplied input can guide through the identification of a subset of features deemed relevant for an adequate assessment of the star metallicity.

We chose metallicity as the target because it can be inferred from well-defined absorption lines of metal species. Such lines are, however, generally blended at the resolution of our dataset and in galaxy spectra. A set of "indices", or wavelength regions, have therefore been defined^{34,35}, which are sensitive to various combinations of metallicity, temperature, and gravity. We will compare the feature importances obtained from the machine learning analysis with these classical indices.

As it can be appreciated by looking at the bottom panel in Figure (11), the most pronounced peaks of λ_i (vertical black traits) are aligned to a subset of the defined indices in the stellar spectra (grey shadows). Namely, we observe high importances being associated with the Calcium H and K line (CaII 3934, 3968), Mgb (mostly associated with the MgI triplet 5167, 5173, 5184) and several absorption bands dominated by Fe II (e.g. Fe4384, Fe5015). All of these indices are known to be sensitive to metallicity. From an astrophysical perspective, the Fe bands are generally considered better probes of metallicity than both the Ca H & K absorptions, which are subject to a number of limitations. Namely, the Ca H & K lines are known to also vary as a function of age (which affects the H/K ratio), and the abundance of Calcium, which has a different nucleosynthetic origin than Fe. On the other hand, a combination of Mgb and Fe5270 (together with Fe5335) is generally considered the best tracer of total metallicity^{36,37}, highlighting the success of our network in identifying relevant features. The network attributes some importance to the H β absorption line but not to H α , as expected given that H β has a larger metallicity dependence than the other Balmer lines.

The upper-left panel in Figure (11) shows the normalized eigenvalues distribution of the input layer eigenvalues. As for the other examples discussed above, a clear peak is displayed close to zero (note the logarithmic scale on the y-axis) thus implying that several input features play no role for the handled task. In particular, if we compute the prediction error on the test set as a function of the number of spectral lines used as input — ordered according to their corresponding eigenvalues — we observe that the minimum error is reached using only around 30 lines (see the upper-right panel in Figure 11). In other words, the network is able to make accurate predictions by relying on just 0.7% of the input components. The eigenvalues allow hence to identify a subset of relevant input elements that drive decision making across the network. In this respect, the algorithm is thus successfully tested against a real dataset with non trivial physical implications.

4 Discussion

We have here elaborated on a procedure for feature relevance extraction, which is founded on solid mathematical grounds. The interest of the proposed method resides in that the user is not asked to decide a priori on what it is relevant or not. The assessment on the actual relevance of the provided input feature follows the evaluation of a scalar indicator (one for each of the features) that self consistently gauges the impact of the supplied information in the decision making problem. These parameters are mathematically traced back to the eigenvalues of the transfer operator linking the first two layers. The method is hence capable of self-adjusting to the specific problem under inspection, with no need for ad hoc (possibly biased) input from external operators.

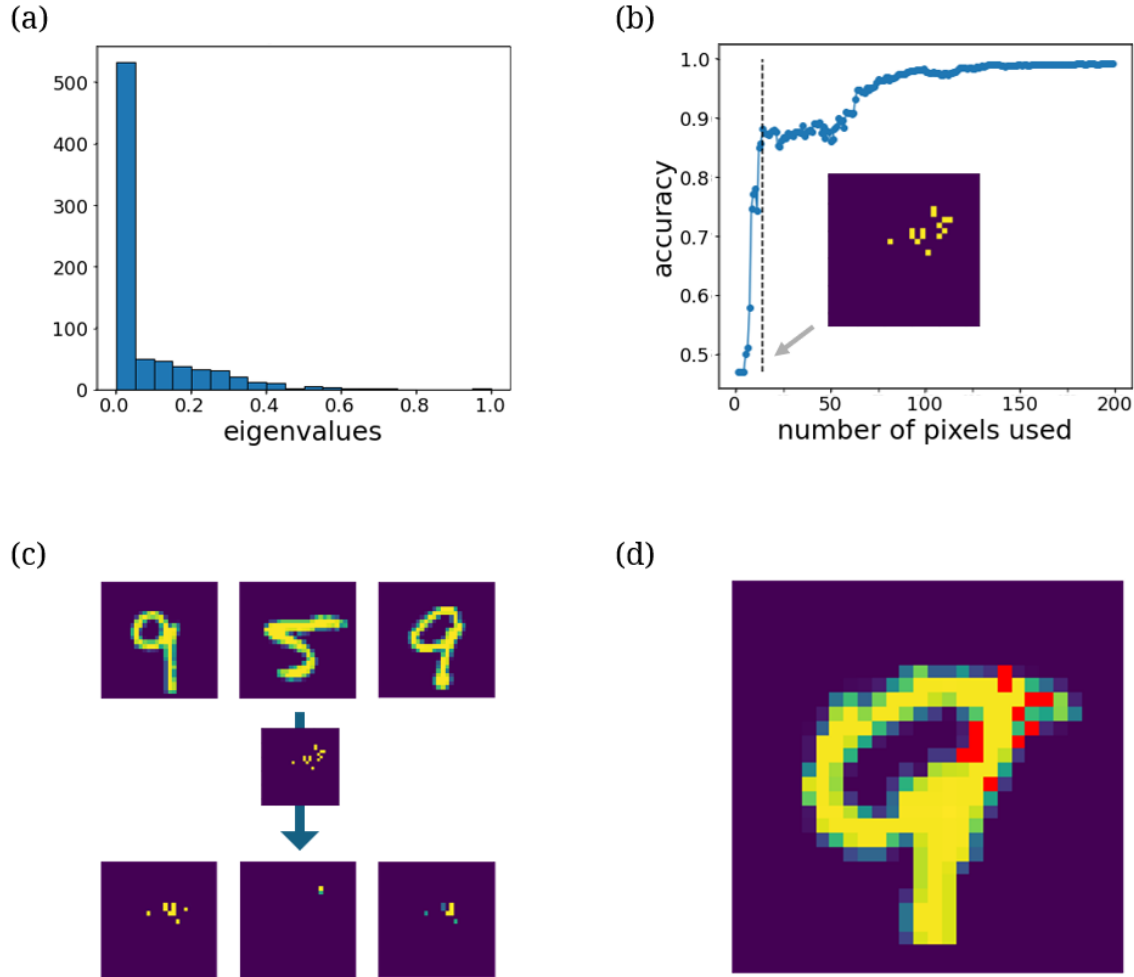


Figure 8. Results for the "five" vs. "nine" case. The neural network was trained to distinguish between images representing the number five and those representing the number nine. Panel (a) displays the distribution of eigenvalues at the end of the training process. A significant peak at zero is observed, indicating that many pixels are not employed for solving the task. Panel (b) illustrates the accuracy trend as a function of the number of pixels provided to the network as input, as follows the reported spectral ranking. Panel (c) presents three example inputs along with the pixels activated after applying the minimal mask. Panel (d) highlights a specific input case where the pixels belonging to the minimal mask and activated for the considered input are marked in red.

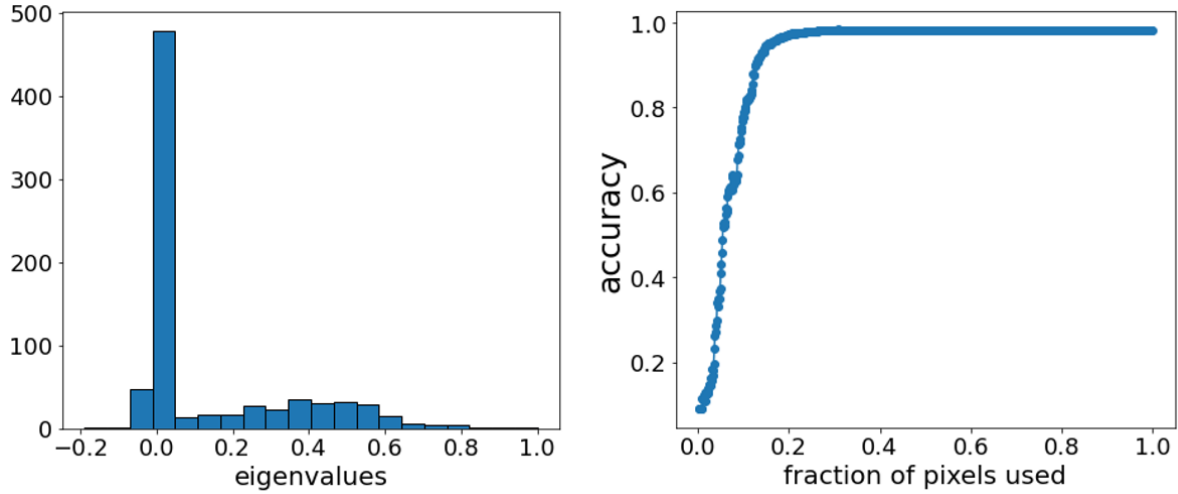


Figure 9. Eigenvalue distribution after training for the full MNIST case (left) and accuracy of the model as the number of pixels taken as input grows (right). The order in which the pixels are inserted follows the absolute value (magnitude) of their corresponding post-training eigenvalues

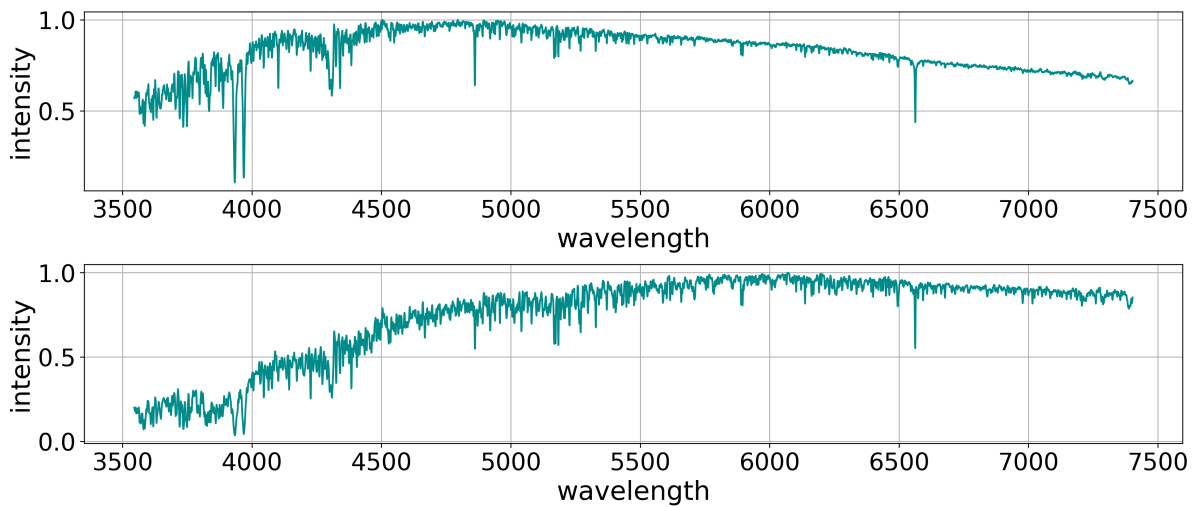


Figure 10. Plot of some of the stellar spectra composing the MILES dataset³⁰.

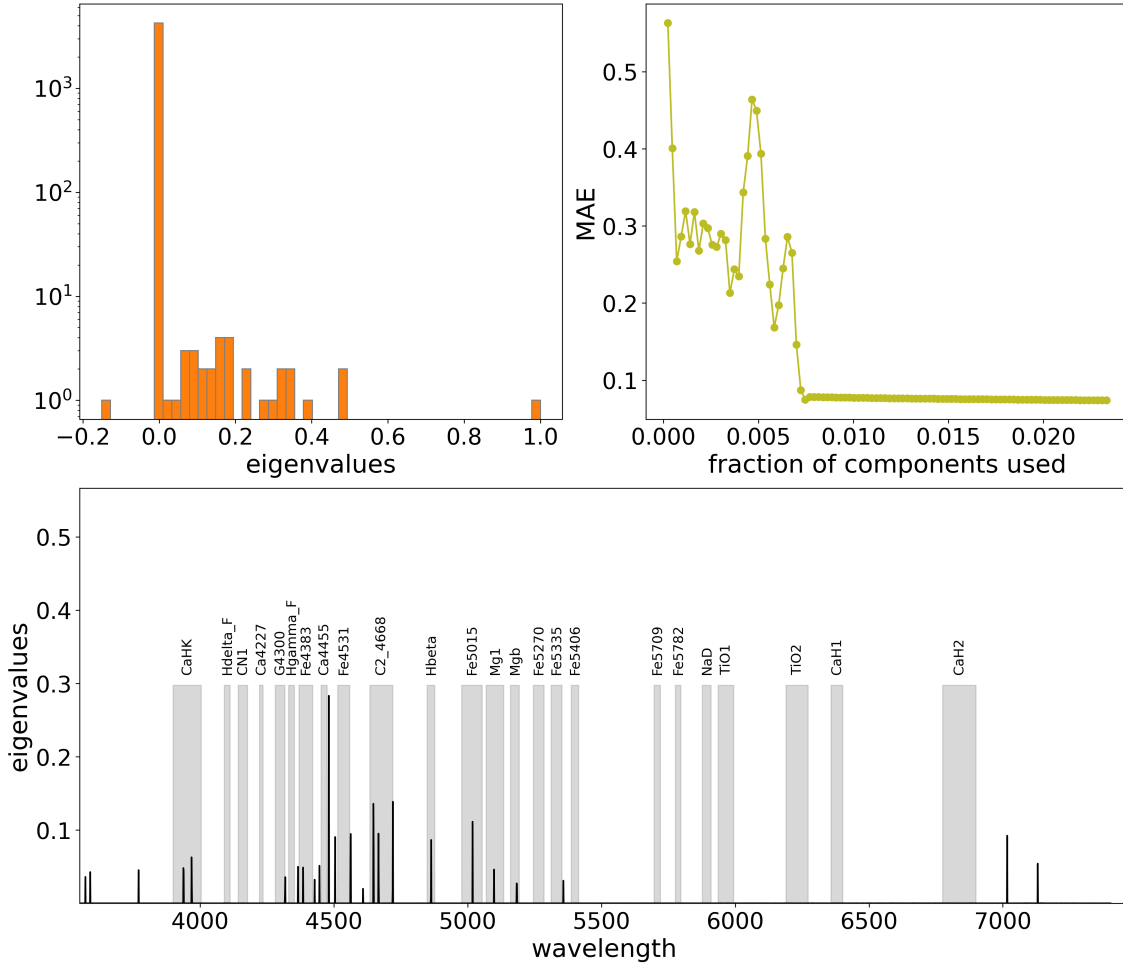


Figure 11. In the upper-left panel the normalized distribution of the eigenvalues of the input layer for the metallicity prediction task is reported in vertical log scale. Upper-right panel shows the mean absolute error of the model versus the fraction of spectral lines provided as an input. The order in which the lines are inserted follows the absolute value (magnitude) of their corresponding post-training eigenvalues. The bottom panel shows the wavelength ranges in the stellar spectra which are deemed relevant for the metallicity prediction task (grey shadows) along with the first layer eigenvalues (see also Method section)

Based on the above reported analysis carried out for both mock and real data, we can positively conclude on the adequacy of the proposed features' detection algorithm. The eigenvalues associated to the input nodes of the collection provide indeed a sensible ranking of the input features.

By working with a relatively simple dataset, we could elaborate on a sound interpretation, drawn a posteriori, of the process that underlying decision making. This includes to *visually* isolate the relevant patches of information that are selectively *seen* by the trained device in operation mode. For more complex datasets, the posterior interpretation could be less transparent in terms of grasping the qualitative message delivered. As an obvious corollary of the analysis, the method could be also applied as a compression algorithm to store large data in a minimal memory kernel.

5 Methods

Spectral Formulation We provide here a few additional details on the spectral approach to the training²². As mentioned in the main body of the paper we consider layer $l-1$ and layer l , respectively made of N and M nodes. The state of the system on layer $l-1$ is encapsulated in vector $\mathbf{x}^{l-1} = (x_1^{l-1}, \dots, x_N^{l-1})$. The state on layer l is instead stored in vector $\mathbf{x}^l = (x_1^l, \dots, x_M^l)$. The mapping is implemented as $\mathbf{x}^l = f(W\mathbf{x}^{l-1})$, where W is a $M \times N$ matrix and f . The spectral recipe deals with the equivalent transformation $\mathbf{z}^l = f(A\mathbf{z}^{l-1})$, where $\mathbf{z}^{l-1} = \mathbf{x}^{l-1} = (x_1^{l-1}, x_2^{l-1}, \dots, x_N^{l-1}, 0, 0, \dots, 0)$ and the last M elements of vector \mathbf{z}^l refer to the actual activity displayed on layer l . An appropriate projection matrix should be formally considered at the end of each mapping between consecutive layers, which effectively implements the transfer of the activations from bottom to upper elements (while filling the bottom portion of the vector with zeros) of the next vector to be processed.

As anticipated in the main body of the paper $A = \Phi\Lambda\Phi^{-1}$ where Φ and Λ are $M \times N$ matrices. The first identifies the eigenvectors of A , the latter the associated eigenvalues. More explicitly we assume:

$$\Phi = \begin{pmatrix} \mathbb{I}^{N \times N} & 0 \\ \Psi & \mathbb{I}^{M \times M} \end{pmatrix}, \quad (4)$$

and:

$$\Lambda = \begin{pmatrix} \lambda_1 & & & \\ & \lambda_2 & & \\ & & \ddots & \\ & & & \lambda_{N+M} \end{pmatrix} \quad (5)$$

As already recalled it can be proven that $\Phi^{-1} = 2\mathbb{I} - \Phi$ ^{23,26}. By making use of this latter expression, it is immediate to show that:

$$A = \begin{pmatrix} \lambda_1 & & & & & \\ & \lambda_2 & & & & \\ & & \ddots & & & \\ & & & 0 & & \\ & & & & \lambda_N & \\ & & & & & \lambda_{N+1} \\ & \boxed{W} & & & & \ddots \\ & & & & & & \lambda_{N+M} \end{pmatrix}. \quad (6)$$

The part of A responsible of the information transfer from the departure layer $l-1$ to the destination layer l is the the bottom-left block W . The relation between the elements of W and the spectral parameters (i.e., the non-zero elements of the matrix Λ and the elements of the Ψ block of the eigenvector matrix) can be analytically computed yielding

$$w_{i \rightarrow j} = w_{ji} = (\lambda_i - \lambda_j) \psi_{ji}. \quad (7)$$

The weights w_{ij} , (associated in the standard formulation to the links of the feedforward network to be trained) are now functions of the spectral attributes of matrix A . Following this alternative parameterization, the target of the optimization are the components and the eigenvectors and the corresponding eigenvalues. From optimized eigenvectors and eigenvalues one can compute the weight of the transfer matrix in direct space via equation (7). The markers used for discriminating relevant

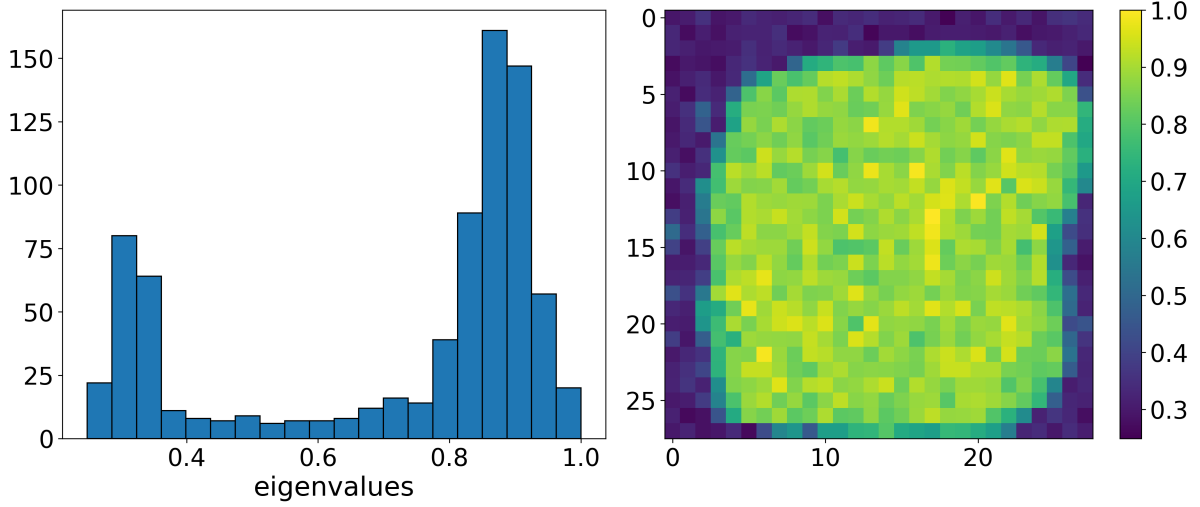


Figure 12. Distribution of the first layer eigenvalues for the MNIST dataset for a model trained with a smaller number of epochs (left) and spatial distribution of the eigenvalues on the input space (right).

features are the eigenvalues of A rescaled by a quantity that accounts for the norm of the associated eigenvectors. In formulae, $\tilde{\lambda}_i = \lambda_i (\sum_j \phi_{ji})^{1/2}$. All along the paper we drop the tilde and refer to $\tilde{\lambda}_i$ as to the i -th eigenvalue of matrix A .

Training procedure The optimization process for all three datasets discussed in the main text was conducted using the Adam optimizer³⁸. The learning rates were set to 0.01 for the first two datasets, 0.0001 for MNIST and 0.001 for the stellar dataset. Sparse Categorical Crossentropy was employed as the loss function for the three classification tasks, while the mean absolute error was used as loss function for the metallicity prediction task. For all tasks under consideration, we applied regularization to both the eigenvalues and eigenvectors of the first layer. The regularization coefficients were set to 10^{-2} for the eigenvalue term and 10^{-4} for the eigenvector term. The number of epochs was set to 1000 for the Gaussian dataset, 500 for the correlated Gaussian dataset, 5000 for MNIST and 1000 for the stellar spectra dataset. Using a large number of training epochs allows us to significantly reduce the regularization term associated with the eigenvalues in the loss function. This, in turn, enables the model to converge to a solution that relies on a minimal subset of input features while still correctly classifying the data. Such sparsity in the input improves the interpretability of the model. It is important to note that employing a large number of epochs is not a stringent requirement: even when operating with fewer training epochs or smaller regularization terms, the eigenvalues of the input layer remain valid indicators of node relevance. However, under these conditions, the model tends to distribute importance across a larger number of input components. While this still yields accurate classification, the interpretation of the internal representations becomes more diffuse and less localized.

As empirical evidence of the above, we report the results for the MNIST dataset and the stellar dataset as obtained for a smaller number of training epochs and reduced regularization factors. By significantly reducing the number of epochs during training on the MNIST dataset, we find a bimodal distribution for the eigenvalues that refer to the input layer with a peak close to zero that is less pronounced as compared to that reported in Sec. (3.3), and a prominent bulk in the region of larger values (See left panel of Fig. 12). This indicates that a greater number of input components are being used to solve the task. By examining the spatial distribution of the eigenvalues, we observe that the relevant components are spread across nearly the entire image (See right panel of Fig. 12). In Figure (13) the results obtained for the stellar dataset are displayed: the eigenvalues associated to the input layer are plotted (black vertical lines) for a model trained with 100 epochs and a regularization coefficient for the eigenvalues set to 5×10^{-4} . The test loss at the end of the training is essentially the same as that obtained for the case reported in Sec. (3.4) (not shown). However, the number of non-zero eigenvalues in the first layer is larger, although most of the peaks still lie in spectral regions known to be crucial for metallicity prediction. In other words the network detected another equivalent solution that makes use of a larger set of input components. 12). We also evaluated the effect of different settings for other hyperparameters, such as the number of layers, the use of batch normalization, and the application of dropout. We did not observe any significant changes in the results under these variations. We would like to recall that our method is input-independent as it does not rely on the activation of the nodes to estimate their relevance (unlike methods such as LRP, for example). Additionally, the eigenvalues of the input layer are parameters directly tied to the input components and

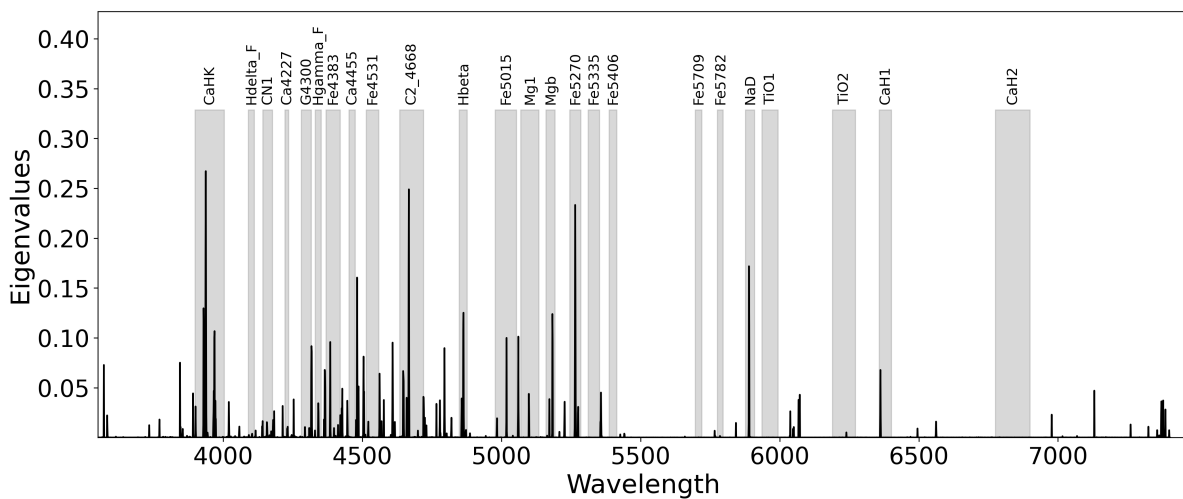


Figure 13. First layer eigenvalues obtained with fewer training epochs and a smaller regularization coefficient (black vertical lines), shown alongside the indices in the stellar spectra considered relevant for the metallicity prediction task (grey shadows)

are unaffected by operations applied in the subsequent layers of the network. For these reasons, our method demonstrates strong robustness to architectural changes and to the use of techniques like batch normalization or dropout. Therefore, the hyperparameters were manually optimized from a restricted set of possible candidates by assessing the model's performance on a validation set (10 % of the training set).

References

1. Deng, L., Yu, D. *et al.* Deep learning: methods and applications. *Foundations trends signal processing* **7**, 197–387 (2014).
2. Goodfellow, I., Bengio, Y. & Courville, A. *Deep learning* (MIT press, 2016).
3. LeCun, Y., Bengio, Y. & Hinton, G. Deep learning. *nature* **521**, 436–444 (2015).
4. Prince, S. J. *Understanding Deep Learning* (MIT press, 2023).
5. Carleo, G. *et al.* Machine learning and the physical sciences. *Rev. Mod. Phys.* **91**, 045002 (2019).
6. Chmiela, S. *et al.* Machine learning of accurate energy-conserving molecular force fields. *Sci. advances* **3**, e1603015 (2017).
7. Chicchi, L., Bindi, L., Fanelli, D. & Tommasini, S. Frontiers of thermobarometry: Gaia, a novel deep learning-based tool for volcano plumbing systems. *Earth Planet. Sci. Lett.* **620**, 118352 (2023).
8. Biancalani, T. *et al.* Deep learning and alignment of spatially resolved single-cell transcriptomes with tangram. *Nat. methods* **18**, 1352–1362 (2021).
9. Baldi, P., Sadowski, P. & Whiteson, D. Searching for exotic particles in high-energy physics with deep learning. *Nat. communications* **5**, 4308 (2014).
10. Guyon, I. & Elisseeff, A. An introduction to variable and feature selection. *J. machine learning research* **3**, 1157–1182 (2003).
11. Bach, S. *et al.* On pixel-wise explanations for non-linear classifier decisions by layer-wise relevance propagation. *PloS one* **10**, e0130140 (2015).
12. Montavon, G., Binder, A., Lapuschkin, S., Samek, W. & Müller, K.-R. Layer-wise relevance propagation: an overview. *Explain. AI: interpreting, explaining visualizing deep learning* 193–209 (2019).
13. Böhle, M., Eitel, F., Weygandt, M. & Ritter, K. Layer-wise relevance propagation for explaining deep neural network decisions in mri-based alzheimer's disease classification. *Front. aging neuroscience* **11**, 194 (2019).

14. Yang, Y., Tresp, V., Wunderle, M. & Fasching, P. A. Explaining therapy predictions with layer-wise relevance propagation in neural networks. In *2018 IEEE International Conference on Healthcare Informatics (ICHI)*, 152–162 (IEEE, 2018).
15. Lundberg, S. A unified approach to interpreting model predictions. *arXiv preprint arXiv:1705.07874* (2017).
16. Sundararajan, M., Taly, A. & Yan, Q. Axiomatic attribution for deep networks. In *International conference on machine learning*, 3319–3328 (PMLR, 2017).
17. Ribeiro, M. T., Singh, S. & Guestrin, C. "why should I trust you?": Explaining the predictions of any classifier. In *Proceedings of the 22nd ACM SIGKDD International Conference on Knowledge Discovery and Data Mining, San Francisco, CA, USA, August 13-17, 2016*, 1135–1144 (2016).
18. Shrikumar, A., Greenside, P. & Kundaje, A. Learning important features through propagating activation differences. In *International conference on machine learning*, 3145–3153 (PMLR, 2017).
19. Swartout, W. R. & Moore, J. D. Explanation in second generation expert systems. In *Second generation expert systems*, 543–585 (Springer, 1993).
20. Montavon, G., Samek, W. & Müller, K.-R. Methods for interpreting and understanding deep neural networks. *Digit. signal processing* **73**, 1–15 (2018).
21. Baehrens, D. *et al.* How to explain individual classification decisions. *The J. Mach. Learn. Res.* **11**, 1803–1831 (2010).
22. Giambagli, L., Buffoni, L., Carletti, T., Nocentini, W. & Fanelli, D. Machine learning in spectral domain. *Nat. communications* **12**, 1330 (2021).
23. Chicchi, L. *et al.* Training of sparse and dense deep neural networks: Fewer parameters, same performance. *Phys. Rev. E* **104**, 054312 (2021).
24. Chicchi, L., Fanelli, D., Giambagli, L., Buffoni, L. & Carletti, T. Recurrent spectral network (rsn): Shaping a discrete map to reach automated classification. *Chaos, Solitons & Fractals* **168**, 113128 (2023).
25. Chicchi, L., Giambagli, L., Buffoni, L., Marino, R. & Fanelli, D. Complex recurrent spectral network. *Chaos, Solitons & Fractals* **184**, 114998 (2024).
26. Buffoni, L., Civitelli, E., Giambagli, L., Chicchi, L. & Fanelli, D. Spectral pruning of fully connected layers. *Sci. Reports* **12**, 11201 (2022).
27. Giambagli, L., Buffoni, L., Chicchi, L. & Fanelli, D. How a student becomes a teacher: learning and forgetting through spectral methods. *Adv. Neural Inf. Process. Syst.* **36** (2024).
28. Giambagli, L., Buffoni, L., Chicchi, L. & Fanelli, D. How a student becomes a teacher: learning and forgetting through spectral methods. *J. Stat. Mech.: Theory Exp.* **2024**, DOI: [10.1088/1742-5468/ad1bea](https://doi.org/10.1088/1742-5468/ad1bea) (2024).
29. Deng, L. The mnist database of handwritten digit images for machine learning research. *IEEE Signal Process. Mag.* **29**, 141–142 (2012).
30. Sánchez-Blázquez, P. *et al.* Medium-resolution isaac newton telescope library of empirical spectra. *Mon. Notices Royal Astron. Soc.* **371**, 703–718 (2006).
31. Cenarro, A. J. *et al.* Medium-resolution isaac newton telescope library of empirical spectra–ii. the stellar atmospheric parameters. *Mon. Notices Royal Astron. Soc.* **374**, 664–690 (2007).
32. Vazdekis, A. *et al.* Evolutionary stellar population synthesis with miles–i. the base models and a new line index system. *Mon. Notices Royal Astron. Soc.* **404**, 1639–1671 (2010).
33. Vazdekis, A., Koleva, M., Ricciardelli, E., Röck, B. & Falcón-Barroso, J. Uv-extended e-miles stellar population models: young components in massive early-type galaxies. *Mon. Notices Royal Astron. Soc.* **463**, 3409–3436 (2016).
34. Faber, S., Friel, E., Burstein, D. & Gaskell, C. Old stellar populations. ii-an analysis of k-giant spectra. *Astrophys. J. Suppl. Ser. (ISSN 0067-0049)*, vol. 57, April 1985, p. 711-741. **57**, 711–741 (1985).
35. Worthey, G., Faber, S., Gonzalez, J. J. & Burstein, D. Old stellar populations. 5: Absorption feature indices for the complete lick/ids sample of stars. *The Astrophys. J. Suppl. Ser. (ISSN 0067-0049)*, vol. 94, no. 2, p. 687-722 **94**, 687–722 (1994).
36. Thomas, D., Maraston, C. & Bender, R. Stellar population models of lick indices with variable element abundance ratios. *Mon. Notices Royal Astron. Soc.* **339**, 897–911 (2003).
37. Candebat, N. *et al.* Inferring stellar parameters and their uncertainties from high-resolution spectroscopy using invertible neural networks. *Astron. & Astrophys.* **692**, A228 (2024).
38. Kingma, D. P. & Ba, J. Adam: A method for stochastic optimization. In Bengio, Y. & LeCun, Y. (eds.) *ICLR (Poster)* (2015).

Data availability

A public repository has been created containing the code used during the work: https://github.com/Lorenzochicchi/SpectralNNs_for_Input_Relevance. Specifically, the code for generating the synthetic datasets used, the code for training the models, and the code for plotting the images included in the work are provided in the form of notebooks.

Acknowledgements

This work is supported by #NEXTGENERATIONEU (NGEU) and funded by the Ministry of University and Research (MUR), National Recovery and Resilience Plan (NRRP), project MNESYS (PE0000006) "A Multiscale integrated approach to the study of the nervous system in health and disease" (DR. 1553 11.10.2022). We thank Francesco Belfiore and Michele Ginolfi for discussion about the astrophysical implications of our findings.